Naval Research Laboratory

Washington, DC 20375-5320

NRL/MR/6362--20-10,155

Low-Pressure Chemical Vapor Deposition (LPCVD) of Few-Layers Molybdenum Disulfide (MoS_2) Crystals

Daniel S. Choi

NRC Postdoctoral Researcher
Washington, DC

Evgeniya H. Lock

Materials and Sensors Branch
Materials Science and Technology Division

November 24, 2020

REPORT DOCUMENTATION PAGE

Form Approved
OMB No. 0704-0188

1. REPORT DATE *(DD-MM-YYYY)*	**2. REPORT TYPE**	**3. DATES COVERED** *(From - To)*
24-11-2020	NRL Memorandum Report	01 Oct 2019 – 30 Sep 2020

4. TITLE AND SUBTITLE

Low-Pressure Chemical Vapor Deposition (LPCVD) of Few-Layers Molybdenum Disulfide (MoS_2) Crystals

5a. CONTRACT NUMBER

5b. GRANT NUMBER

5c. PROGRAM ELEMENT NUMBER

6. AUTHOR(S)

Daniel S. Choi* and Evgeniya H. Lock

5d. PROJECT NUMBER

5e. TASK NUMBER

5f. WORK UNIT NUMBER
1G71

7. PERFORMING ORGANIZATION NAME(S) AND ADDRESS(ES)

Naval Research Laboratory
4555 Overlook Avenue, SW
Washington, DC 20375-5320

8. PERFORMING ORGANIZATION REPORT NUMBER

NRL/MR/6362--20-10,155

9. SPONSORING / MONITORING AGENCY NAME(S) AND ADDRESS(ES)

10. SPONSOR / MONITOR'S ACRONYM(S)

11. SPONSOR / MONITOR'S REPORT NUMBER(S)

12. DISTRIBUTION / AVAILABILITY STATEMENT

DISTRIBUTION STATEMENT A: Approved for public release; distribution is unlimited.

13. SUPPLEMENTARY NOTES

*NRC Postdoctoral Researcher, 500 Fifth Street, N.W., Washington, DC 20001.

14. ABSTRACT

Two-dimensional (2D) molybdenum disulfide (MoS_2) is a highly promising material for various 2D and quantum-enabled applications due to its excellent electrical and optical properties such as mobility of 200 – 700 $cm^2V^{-1}s^{-1}$, fast on/off switch ratio of 10^7, and high photoresponsivity of 7.5 mA/W under low illumination power (80 μW). Thus, a large-scale high-quality material is needed for the next technological breakthrough. In this report, we show a Low-Pressure Chemical Vapor Deposition (LPCVD) synthesis of MoS_2 crystals on silicon substrates. A systematic optimization of the growth parameters, including precursor powders quantity, temperature, pressure, the relative positions of the precursors' components, and the substrate orientation resulted in control of MoS_2 crystal thickness. The presented work provides the basis not only for developing a large-scale MoS_2 films but it can also be applied to synthesize other transition metal dichalcogenide materials and their heterostructures.

15. SUBJECT TERMS

Quantum technology
Molecular rotors
Self assembled monolayers
Two level systems

16. SECURITY CLASSIFICATION OF:			**17. LIMITATION OF ABSTRACT**	**18. NUMBER OF PAGES**	**19a. NAME OF RESPONSIBLE PERSON**
a. REPORT	**b. ABSTRACT**	**c. THIS PAGE**			Evgeniya H. Lock
Unclassified Unlimited	Unclassified Unlimited	Unclassified Unlimited	Unclassified Unlimited	28	**19b. TELEPHONE NUMBER** *(include area code)* (202) 767-0351

Standard Form 298 (Rev. 8-98)
Prescribed by ANSI Std. Z39.18

This page intentionally left blank.

Low-Pressure Chemical Vapor Deposition (LPCVD) of Few-Layers Molybdenum Disulfide (MoS_2) Crystals

Daniel S. Choi* and Evgeniya H. Lock#
*National Research Council Postdoctoral Fellow in residence at the Naval Research Laboratory, Washington DC 20375
#Materials Science and Technology Division, Naval Research Laboratory, Washington DC 20375

ABSTRACT

Two-dimensional (2D) molybdenum disulfide (MoS_2) is a highly promising material for various 2D and quantum-enabled applications due to its excellent electrical and optical properties such as mobility of 200 – 700 $cm^2V^{-1}S^{-1}$, fast on/off switch ratio of 10^7, and high photoresponsivity of 7.5 mA/W under low illumination power (80 µW). Thus, a large-scale high-quality material is needed for the next technological breakthrough. In this report, we show a Low-Pressure Chemical Vapor Deposition (LPCVD) of MoS_2 crystals on silicon substrates. A systematic optimization of the growth parameters, including precursor powders quantity, temperature, pressure, the relative positions of the precursors' components, and the substrate orientation resulted in control of MoS_2 crystal thickness. The presented work provides the basis not only for developing a large-scale MoS_2 films but it can also be applied to synthesize other transition metal dichalcogenide materials and their heterostructures.

1. INTRODUCTION

a) Application of MoS_2

Molybdenum disulfide (MoS_2), a semiconducting transition metal dichalcogenide (TMD), is a highly explored material due to its unique electronic and optical properties. In the bulk structure, MoS_2 crystal is an indirect bandgap semiconductor with bandgap energy (E_g) of 1.2 eV[1], while monolayer, two-dimensional (2D) MoS_2 crystal is a direct bandgap semiconductor with a bandgap of 1.8 eV[2]. In a monolayer MoS_2 structure, molybdenum (Mo) and sulfur (S) atoms are covalently bonded. They are arranged in a zigzag like geometry in an S-Mo-S unit, as seen in Figure 1a. In a layered structure, the distance between two planes of MoS_2 is 0.653 nm and is stabilized by van der Waals interaction between the S atoms[3]. Due to the unique bandgap transition observed from bulk to nanoscale, two-dimensional MoS_2 films have demonstrated unique electrical properties such as mobility of 200 - 700 $cm^2V^{-1}S^{-1}$ and high current on/off ratio 10^5 – 10^7 [4–6]. Additionally, as the indirect-direct bandgap transition is induced by a strong quantum confinement effect, monolayer to few-layers MoS_2 films exhibit strong photoluminescence properties with high quantum yield, including single-photon emission[7] making it a highly promising material for applications in photonic, optoelectronic, sensors, and photodetectors[8–15].

Manuscript approved November 23, 2020.

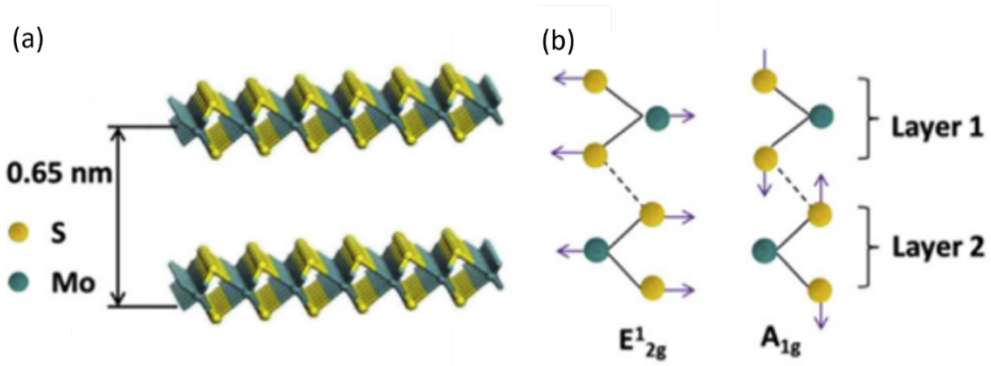

Figure 1. Crystal structure of two-dimensional MoS_2. (a) shows the Mo and S atomic planes of two-layer MoS_2 as well as the distance between two MoS_2 layers while (b) shows two Raman active, in-plane (E^1_{2g}) and out of the plane (A_{1g}) intralayer modes. It was reproduced without permission from Li[16].

MoS_2 films have become increasingly important in the production of van der Waals heterostructures in which different classes of 2D materials are brought together to develop hybrid systems with unique material properties[16]. For instance, while MoS_2 has shown to have outstanding current switching properties, its relatively lower mobility (compared to graphene) prevents the fabrication of MoS_2 exclusive electrodes and devices. However, when MoS_2 is combined with high mobility material such as graphene, a new device based on both materials is now possible. As such, to advance two-dimensional enabled MoS_2-hybrid applications, a reliable synthesis methodology for MoS_2 films must be first developed, and it is the focus of this report. The following sections will discuss the advantages and limitations of various MoS_2 synthesis approaches.

b) MoS_2 synthesis methods

The two main approaches for synthesizing two-dimensional MoS_2 crystals and films are (1) top-down such as exfoliation, and (2) bottom-up approaches such as molecular beam epitaxy (MBE) and chemical vapor deposition (CVD). The exfoliation methods include mechanical and chemical processes to remove thin MoS_2 flakes or crystals from a bulk crystal. Similar to the "Scotch tape method" utilized in graphene synthesis[17], larger MoS_2 crystals are mechanically cleaved to produce high quality, monolayer films or flakes[18]. However, this method is not suitable for device or industry scale applications because of its low yield, small micrometer-scale size, and difficulties in layer control. Chemical exfoliation, on the other hand, utilizes intercalation, i.e., insertion of atoms into layered structures, to exfoliate nanosheets from bulk MoS_2 crystals[19]. For instance, in lithium intercalation, lithium ions are inserted into MoS_2 crystals results in the exfoliation of MoS_2[20]. However, the materials produced by this method have metallic impurities limiting its device potential. Another chemical exfoliation approach is via the Coleman method[21]. In this method, a bulk MoS_2 crystal is suspended in an organic solvent then sonicated to achieve a layered structure. By controlling the sonication parameters, flakes of various layers are achieved. This method produces a higher yield than the mechanical exfoliation. However, the sonication often causes defects to the 2D lattice and reduces the flake size (a few thousand nanometers), limiting its usage in the device applications[16].

The "Bottom-up" synthesis approach of the molecular beam epitaxy is an advanced technique for growing thin-film layers of MoS_2 crystals directly on the substrate. In MBE synthesis, molybdenum and sulfur precursors are evaporated under high vacuum and deposited onto a target substrate. The growth and expansion of thin-film are divided into two main processes[22]: (1) Formation of scattered domains and (2) Expansion and stitching of domains to form a film. Typically for MoS_2 film growth, the first stage takes approximately 3 to 4 hours to complete at ~750 ºC while the second stage takes about 6 to 7 hours at ~900 ºC. While MBE produces high-quality, uniform films, MBE requires complex and expensive equipment to operate. Furthermore, due to the slow crystal growth rate (few microns per hour), combined with the time needed for the vacuum (10^{-8} Torr), the process is slow and is low-throughput compared to the alternative bottom-up approach. Additionally, there have been reports of transitional metal dichalcogenides (TMDs) synthesized via MBE to have limited grain size (< 200 nm), which limits its usage in producing 2D materials for device fabrication[23,24].

As such, an alternative, bottom-up synthesis CVD approach has shown promise for producing defect-free, layer controlled, high-yield, MoS_2 crystals and films at a technologically relevant scale. CVD approaches have the potential for direct growth of heterostructures removing the need for the multi-step, layer-by-layer buildup of layers, which is often associated with interlayer contamination[16]. Chemical vapor deposition synthesis methods for MoS_2 can be divided into three major groups: (1) Vapor-solid growth, (2) Sulfurization of the molybdenum-based compound, and (3) Pre-deposition of molybdenum on the substrate, followed by sulfurization of molybdenum-based oxides.

Vapor-solid growth methods utilize MoS_2 powder as the precursor for MoS_2 growth[25]. This approach produced large triangular flakes of MoS_2 in approximately 25 μm size with room temperature photoluminescence properties comparable to mechanically exfoliated flakes. However, due to the tendency for random nucleation of MoS_2 crystals and the formation of MoS_2 islands, consistent uniform growth of films is not yet achieved.

Synthesis of MoS_2 films via sulfurization of Mo compounds utilizes molybdenum trioxide (MoO_3) and sulfur (S) powders as solid precursors. They are vaporized and then nucleated on a SiO_2/Si substrate. Typically, the growth is carried out in an ambient environment. Atomic force microscope (AFM) analysis of MoS_2 crystals produced by this method shows that their thickness of 0.72 nm is comparable to monolayer exfoliated MoS_2 flakes[26,27]. The electrical properties of MoS_2 films produced via this method are excellent, with current switching ratio of 10^4. Further modifications have been made, such as conducting the growth under lower pressure and substituting MoO_3 with molybdenum chloride ($MoCl_5$) to produce centimeter-scale films[12].

Another method of MoS_2 synthesis is by first pre-depositing a thin layer of molybdenum (1-5 nm) on SiO_2/Si via e-beam evaporation then react in a CVD furnace with MoO_3 and S as the precursors[28]. While this method produced uniform MoS_2, the film thickness was approximately 2 nm, thicker than a true monolayer MoS_2[29]. Additionally, the film produced by this method exhibited resistor-like behavior, with a sheet resistant value of 10^4 Ω/sq and a low mobility value of 0.004-0.04 $cm^2V^{-1}S^{-1}$ limiting its use in devices and applications[28].

While all three types of CVD methods have been extensively achieved in atmospheric pressure, Low-Pressure Chemical Vapor Deposition (LPCVD) is the preferred growth approach because it reduces the unwanted gas-phase moisture controlled reaction, as well as minimizing nuclei density, leading to better-quality, uniform, large-area MoS_2 film deposition[12,30,31]. As such, the objective of this work to develop a protocol for LPCVD synthesis of two to three layers thick MoS_2 crystals and films on SiO_2/Si substrates via sulfurization of MoO_3 and S powders as

precursors. The LPCVD growth approach was developed by optimizing the (1) precursors amount, (2) growth pressure, (3) relative position of the growth substrate with respect to the precursors, and (4) the utilization of an external heating element for S sublimation. After each growth, the quality of the MoS_2 film growth was verified by optical microscopy and Raman spectroscopy. Additionally, Raman analysis of the two Raman active vibrational modes (E^1_{2g} and A_{1g}) was performed to estimate the thickness, i.e., the number of layers of the MoS_2. The developed growth technology and the accompanying analysis presented in this report can be applied to the growth of other TMD materials such as WSe_2 and WS_2 and provide a basis for developing direct synthesis methods for TMD/graphene hybrid structures for advancing materials research in quantum applications[32].

2. EXPERIMENTAL

2.1 Chemical Vapor Deposition (CVD) Chamber

Synthesis of MoS_2 crystals was carried out in a three-temperature zone chemical vapor deposition (CVD) reactor furnace (Model# OTF-1200X-III-S, MTI Corporation). The reactor furnace (Figure 2) consisted of a 122 cm long, 10.16 cm outer-diameter quartz tube placed in three independently controlled temperature zones with 16 cm, 30 cm, and 16 cm length respectively (Figure 2). Approximately 30 cm of the quartz tube is overhung at both ends and not directly exposed to the heating elements of the furnace. An additional heating belt (Omega Engineering SWH171-020) was wrapped around the exposed part of the tube next to at the Zone 3/entrance to sublimate the S powder precursor. The carrier gas argon (Ar) was controlled via a mass flow controller (MKS Type 1179A) and flowed from Zone 3 to Zone 1 during the synthesis to keep the system oxygen and moisture-free and to carry the precursor vapors. The outlet, at the left of Zone 1, was connected to a molecular pump (MTI Corporation) to keep the reaction chamber under low-pressure and to drive out the precursor vapor.

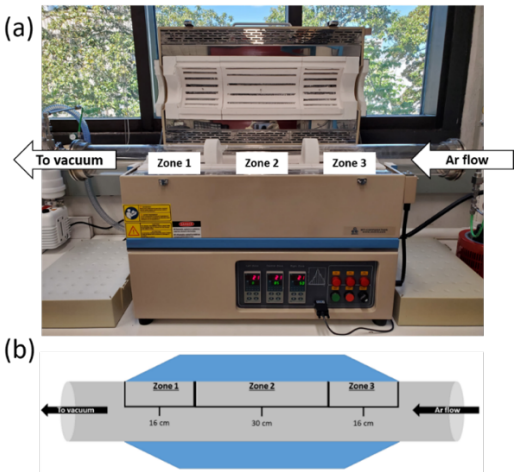

Figure 2. (a) CVD reactor oven used for MoS_2 synthesis and (b) detailed schematic of the tube furnace indicating dimensions of individual heating zones and direction of the gas flow.

In low-pressure chemical vapor deposition synthesis, it is crucial to monitor the chamber pressure during the growth process. A preliminary study to correlate the internal chamber pressure

to the argon gas flow rates was conducted, and the results are summarized in Table 1 and Figure 3. Both show a linear correlation between the argon gas flow and the internal chamber pressure. Excellent pressure control with a broad pressure range from 38 to 1190 mTorr was achieved by changing the argon flow rates.

Table 1. Internal chamber pressure under various Ar gas flow.

Ar gas flow (sccm)	0	5	15	25	50	75	100	150	200
Chamber pressure (mtorr)	38.4	112	198	286	438	577	715	745	1190

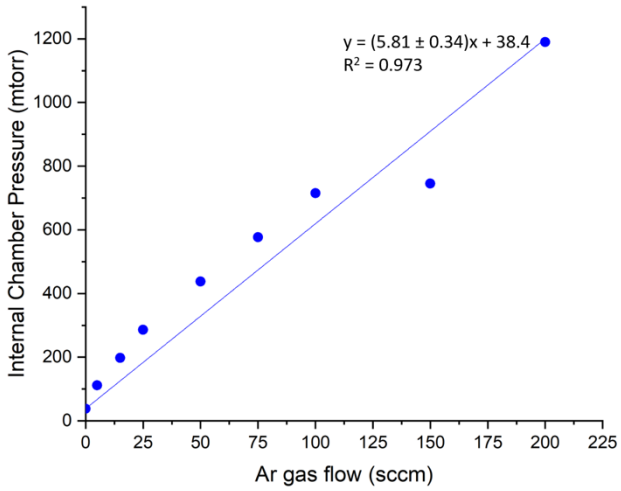

Figure 3. Linear correlation between reactor pressures and argon gas flow rates with a calculated R-squared value of 0.973.

2.2 MoS_2 Synthesis

Chemical vapor deposition growth of MoS_2 crystals consists of sublimation of molybdenum and S precursor powders, which nucleate on the target surface (SiO_2/Si wafers, sapphire, others) under constant carrier gas flow. In this report, 99.9995% purity molybdenum trioxide (MoO_3) and 99.5% purity sulfur (S) powders (Alfa Aesar) powders were utilized as precursors, respectively. The carrier gas used was ultra-high 99.9995 % purity argon (Earlbeck Gases & Technologies). The target substrate was p-type/B-doped, (100) orientation Si wafer with 300 nm thick thermal SiO_2 oxide (MTI Corporation).

First, the SiO_2/Si wafer was cut into smaller, 15 mm x 10 mm pieces. Then, oxygen plasma treatment was performed using an RF plasma system (Plasma Etch) to increase the silicon wafer wettability. Before the substrate treatment, the plasma system was cleaned with ultra-high purity oxygen gas under 15 sccm flow, 50 W, for 10 minutes. The SiO_2/Si substrates were then placed in the chamber and treated via oxygen plasma under 10 sccm O_2 gas flow, at 40 W power, for one minute. Using a Video Contact Angle Optima Goniometer System (AST Products), the surface contact angle of the silicon substrate before and after plasma exposure was determined. The

untreated SiO_2/Si substrate had an average water contact angle (WCA) of 45°, while the post-plasma treated surface showed a completely hydrophilic surface.

Table 2 contains a summary of the experimental conditions for the experiments described in this report. Parameters modified were: (1) Mass of precursor powders, (2) Argon flow rate/chamber pressure, (3) Relative distance between the powder precursors and the target substrate in the reactor, and (4) Effect of the heating belt for S sublimation.

Table 2. Complete experimental parameters set for MoS_2 crystal growth.

Exp. #	Sample ID	Powder		Ar Flow (sccm)	Ramp Time (min)	Growth Time (min)	Chamber Pressure (mTorr)	Temperature (°C)								Distances (cm)			Substrate Orientation
								Zone 1		Zone 2		Zone 3		Heat. belt					
		S (g)	MoO_3 (g)					Set	Final	Set	Final	Set	Final	Set	Final	0-Sulfur	0-MoO_3	0-SiO2/Si	
1	200114A1	1	0.5	50	20	45	377	off	569	850	850	off	552	180	180	15	60.5	58	Down
	200114B1	1	0.5	50	20	45	377	off	569	850	850	off	552	180	180	15	60.5	60.5	Down
2	200114A2	0.5	0.1	50	20	45	368-376	800	798	550	550	180	320	180	180	15	60.5	85	Up
	200114B2	0.5	0.1	50	20	45	368-376	800	798	550	550	180	320	180	180	15	60.5	82	Up
3	200115A1	0.5	0.05	50	20	45	370-381	850	850	850	850	150	554	180	180	15	60.5	60.5	Down
4	200115A2	0.5	0.05	25	20	45	230-247	850	798	850	850	120	554	180	180	15	60.5	60.5	Down
5	200115A3	0.5	0.05	25	20	45	230-240	850	827	600	550	150	557	180	180	15	60.5	83.5	Up
6	200116A1	0.5	0.05	25	20	45	230-244	850	850	850	850	100	555	180	180	15	60.5	60.5	Down
7	200116A2	0.5	0.05	25	20	45	230-244	850	850	850	850	100	555	180	180	15	60.5	60.5	Down
	200116B2	0.5	0.05	25	20	45	228-244	850	850	850	850	100	555	180	180	15	60.5	75.5	Up
8	200116A3	0.5	0.05	25	20	45	228-244	850	850	850	850	180	570	off	off	30	60.5	60.5	Down
	200116B3	0.5	0.05	25	20	45	227-241	850	850	850	850	180	570	off	off	30	60.5	75.5	Up
9	200117B1	0.5	0.05	25	20	45	252-242	850	850	850	850	180	563	off	off	15	60.5	60.5	Down

A schematic diagram of the substrate and precursor arrangement for experiment 1 is shown in Figure 4. Two silicon substrates labeled "A1" and "B1" were facing down. "Spot **0**" is defined as the entrance of the tube furnace and is used as the point of reference for relative positions of the other components. From this point, the S powder, MoO_3 powder and, substrate positions were measured as 15 cm, 60.5 cm, and 58 cm (A1) [60.5 cm (B1)] accordingly. Thus, the relative distance between precursor (S and MoO_3) powders was approximately 46 cm, while the SiO_2/Si substrates were on top of the MoO_3 powder boat, as shown in Figure 4.

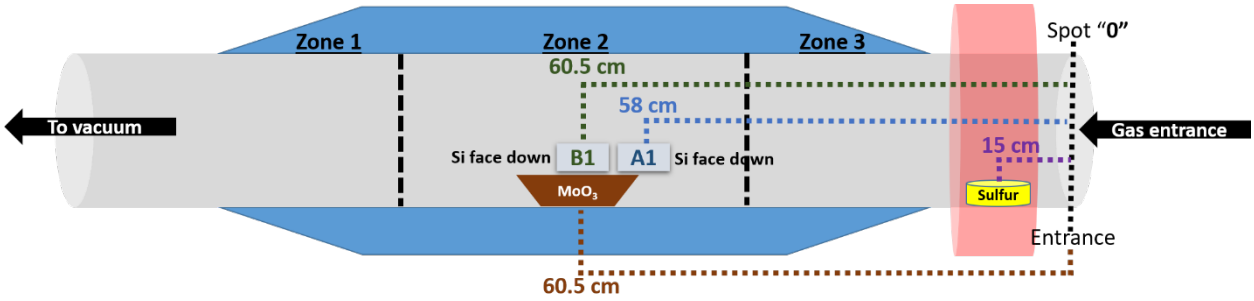

Figure 4. Representative schematic diagram for experiment 1 with relative locations of S, MoO_3, and SiO_2/Si substrates (A1 and B1). The Center of the tube is measured to be 60.5 cm.

For every experiment, a specified amount of S and MoO_3 powders were placed in ceramic boats at selected positions (Table 2). After the plasma treatment, SiO_2/Si substrates were placed in the appropriate positions (Table 2), then both ends of the reactor tube were closed and pumped down to achieve a base pressure of less than 30 mTorr. Argon carrier gas was introduced into the chamber with an appropriate flow rate controlled via a mass flow controller to achieve the desired experimental pressure. The reactor's temperature and its ramping rate for each zone (Figure 4) were controlled via MTI's furnace software. The S sublimation occurs at 180 ºC, while MoO_3 sublimation occurs in the 600 to 850 ºC range. Thus, precise temperature control is needed for both processes. The S powder was placed in the outside portion of the reactor tube, not directly heated by the furnace with a heating belt wrapped around it to facilitate S sublimation.

Typical MoS_2 growth took approximately 70 minutes without considering the reactor cooling. In the first 22 minutes, both S and growth/MoO_3 zones were heated in parallel. After reaching their respective temperatures, all zones were held for 45 minutes - at this phase, the MoS_2 growth occurs. After completing the growth, the furnace was cooled down using fans and opening the top of the furnace. Figure 5 shows a temperature-time profile of each zone during MoS_2 synthesis.

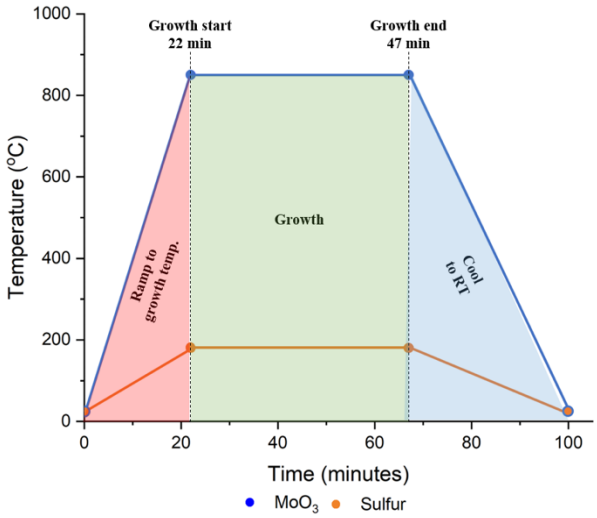

Figure 5. A time-temperature profile of the sulfur zone and growth/MoO_3 zones for the MoS_2 growth experiment. Sublimation of MoO_3 and sulfur occur in parallel for nucleation on the SiO_2/Si substrate during the growth stage.

Upon cooling of the furnace to room temperature, the argon gas flow was stopped, the reactor tube was brought up to atmospheric pressure, and the growth substrates and the precursor ceramic boats removed. Then, the reactor tube was closed and evacuated down to a pressure of approximately 30 mTorr. The SiO_2/Si surface characterization was performed using an optical microscope Olympus BX53M to qualitatively observe MoS_2 crystals or film production. Also, Raman spectroscopy using a Renishaw inVia Raman Microscope equipped with a 514 nm laser was performed to verify MoS_2 crystal formation and estimate the number of MoS_2 crystal layers.

3. RESULTS AND DISCUSSION

3.1 Optical and Raman Characterizations

In the initial experiment, the amounts of precursor powders were 1 g and 0.5 g of S and MoO_3, respectively. The argon flow rate was set to 50 sccm to achieve a growth reactor pressure of 377 mTorr. The temperature of the growth zone (Zone 2, middle of the reactor) was set to 850°C, and the heating belt temperature was used to sublimate the S precursor. The S powder was loaded into a ceramic cup and placed 15 cm from the tube entrance, while the MoO_3 powder was placed in a ceramic boat and placed in the center of the furnace (60.5 cm from the entrance) as described in Figure 4. SiO_2/Si substrates were placed at the center of the tube overhanging the MoO_3 boat facing down at 58 cm and 60.5 cm, respectively, from the tube entrance. Figure 6 shows optical images of thick, non-uniform MoS_2 crystals obtained from this condition. The thick film is attributed to the excess amount of precursor powders leading to heavy deposition of the vapors on substrate surfaces.

The Raman analysis in Figure 7 shows two peaks present around 383 cm^{-1} and 406 cm^{-1}. These values are in agreement with Raman active peaks of bulk MoS_2. As seen in Figure 1b, the two primary Raman active peaks for a monolayer MoS_2 are (1) lower in-plane, E^1_{2g} mode at 382 $cm^{-1,}$ and an out-of-plane, A_{1g} mode at 402 cm^{-1}. The approximately 4 cm^{-1} difference in the out-of-plane mode for our sample indicates significantly more interlayer interactions in the out-of-plane mode showing a thicker structure compared to monolayer MoS_2. A summary of Raman analysis with corresponding average peak position/frequency for all experiments is presented in Table 3. Additionally, the complete set of Raman spectra as with peak position/frequency analysis is presented in detail in the Appendix.

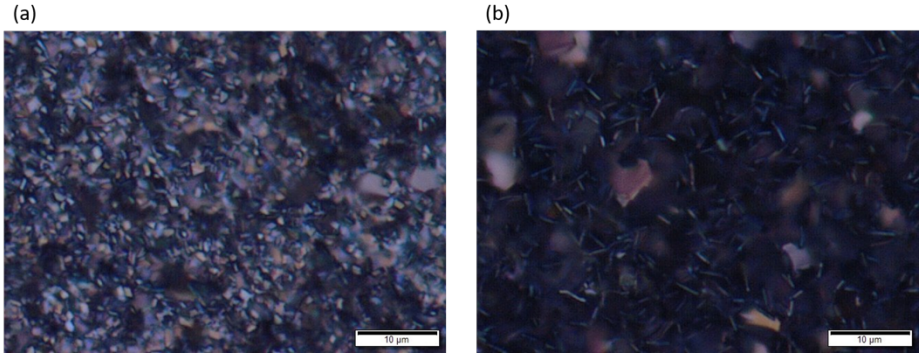

Figure 6. Optical microscope images (100x) of MoS_2 crystals obtained from experiment 1. (a) and (b) correspond to 200114A1 and 200114B1. The scale bar is 10 µm.

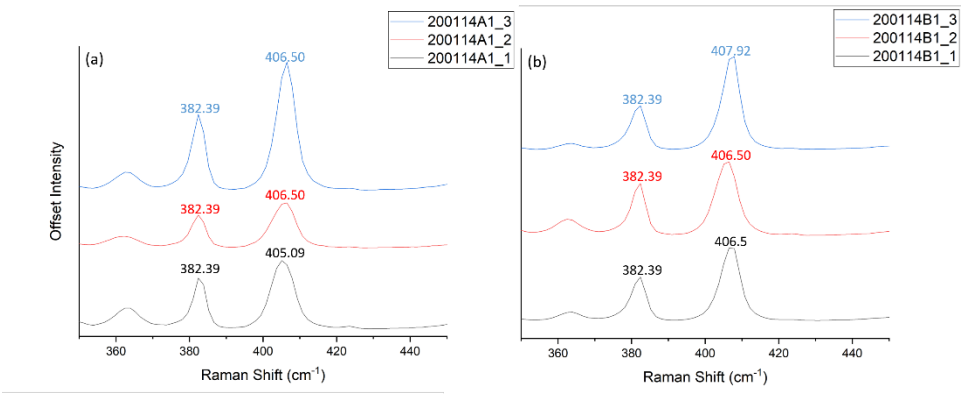

Figure 7. Raman spectroscopy data for experiment 1. (a) corresponds to 200114A1 and (b) corresponds to 200115B1. Different colors represent separate areas analyzed.

Table 3. Summary of the average values of the E^1_{2g} and A_{1g} modes frequencies.

Sample		Exp.	Figure	Peak Frequency (cm^{-1})	
				Avg. E^1_{2g}	Avg. A_{1g}
200114	A1	Exp. 1	6a	382.39	406.03
	B1		6b	382.39	406.97
	A2	Exp. 2	8a	No MoS_2 growth	
	B2		8b	No MoS_2 growth	
200115	A1	Exp. 3	9a	380.97	407.92
	A2	Exp. 4	9b	378.83	404.38
	A3	Exp. 5	9c	No MoS_2 growth	
200116	A1	Exp. 6	9d	380.97	405.78
	A2	Exp. 7	10a	382.39	405.09
	B2		10b	383.10	407.21
	A3	Exp. 8	11a	383.10	405.44
	B3		11b	383.10	406.50
200117	B1	Exp. 9	11c	383.10	405.09

Therefore, to reduce the MoS_2 deposition rate and produce thinner structures, the precursor amounts were decreased by a factor of two and five for S (0.5 g) and MoO_3 (0.1 g) respectively for the subsequent experiments. Additionally, the SiO_2/Si growth substrate was placed further downstream, 21 cm, and 25 cm from the MoO_3 precursor (85 cm from entrance) to reduce the amount of vapor deposited on the substrate surface. Figure 8 shows optical images of the resulting experiment in which no MoS_2 crystal growth occurred. This observation was also confirmed via Raman spectroscopy, as only the silicon substrate peak at 520 cm^{-1} was detected (Figure A1).

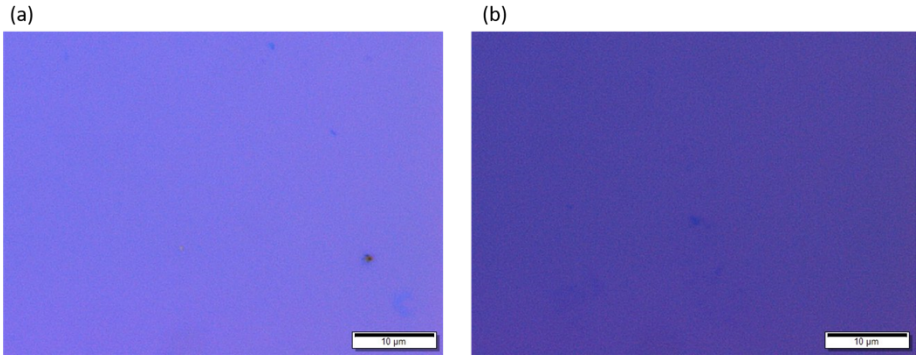

Figure 8. 100x optical microscope images of experiment 2, where the growth substrates were placed further downstream from the precursor powders. (a) and (b) correspond to substrates 200114A2 and 200114B2 substrates, respectively. MoS_2 deposition did not occur for either substrate. The scale bar is 10 µm.

In establishing optimal synthesis parameters such as respective distances between precursors and the substrates, mass of the precursors, and internal chamber pressure, the growth reactor chamber configuration should be taken into account to understand the MoS_2 growth mechanism, as well as the gas and particle deposition kinetics especially when comparing different growth systems. The CVD reactor tube used in this work is relatively large with a diameter (D) and length of 10.16 cm and 122 cm. However, growth chambers used by other research groups have smaller diameters (D = 2.54 – 7.62 cm) and lengths (L < 100 cm)[33–36] and thus many instrument-specific variables such as (1) the extraneous path for vaporized particles to diffuse across the tube, (2) correlation between the gas flow and internal chamber pressure, (3) the probability of nucleation on the SiO_2/Si substrate surface concerning the relative distance, must be determined.

Thus, in the next experiments, we varied the relative positions of the substrates, precursors, and substrate orientation compared to the gas stream. First, the SiO_2/Si substrates were moved from far down-stream in Zone 1 (85 and 82 cm from the gas entrance), to the middle of the reactor tube (60.5 cm from entrance). The positions of the S and MoO_3 precursors remained unchanged (15 cm and 60.5 cm from the entrance, respectively). Furthermore, the mass of the S precursor was kept constant at 0.5 g, while the amount of MoO_3 powder was reduced by a factor of 2 (0.05 g) as thinner MoS_2 deposition is desired. Lastly, the argon flow rate was reduced from 50 to 25 sccm after experiment 3 to achieve an internal chamber pressure of 230 mTorr allowing for more uniform deposition on the substrates[37–39]. The optical images in Figures 9a, 9b, and 9d show a thinner deposition of MoS_2 crystals compared to the thick film observed in Figure 6. This was due to less aggregation of precursor vapors on the substrate surface due to the lower amount of precursor powder utilized as well as to the reduced internal pressure. The Raman analysis shows average peak positions at ~380 – 382 cm^{-1} and ~404 – 407 cm^{-1} for E^1_{2g} and A_{1g}.

Comparing these results with the previous ones presented in Figures 6 and 8, shows the almost complete sublimation of both precursor powders producing near-zero solid waste. Additionally, Figure 9c shows results from the same growth conditions with different locations of the growth substrates compared to the MoO_3 precursor powders (83.5 cm downstream compared to 60.5 cm for Figures 9a, 9b, and 9d). However, with this placement, no MoS_2 crystal growth was detected, as verified by a lone silicon peak at 520 $cm^{-1,}$ indicating the importance of the growth substrate placement with respect to the precursor powders.

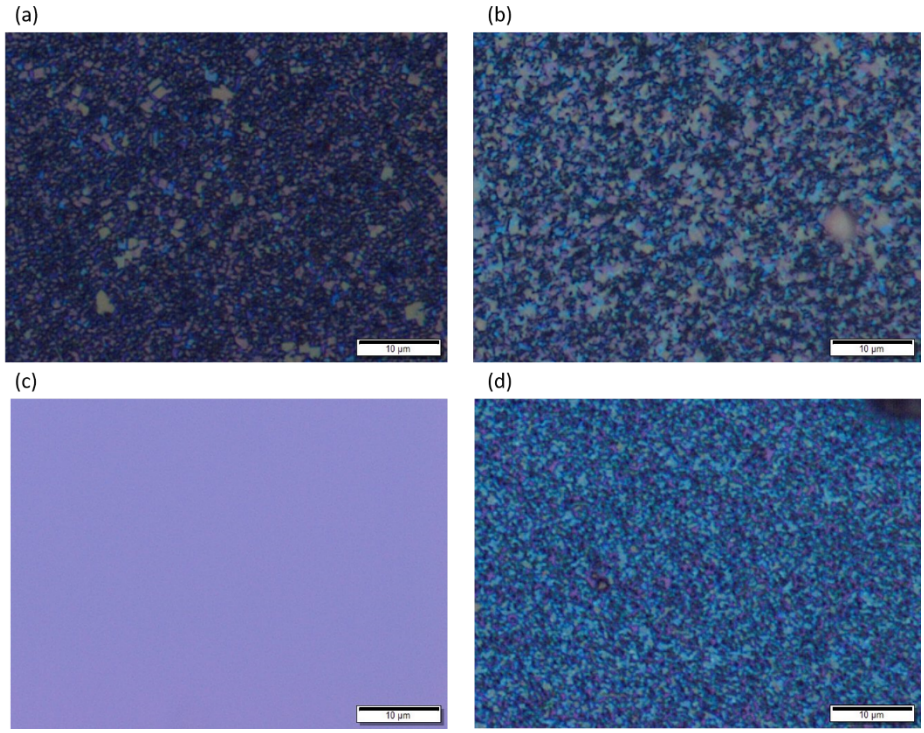

Figure 9. 100x optical microscope images of MoS_2 crystal growth from experiments 3 – 6 in which the amount of MoO_3 and internal chamber pressure were reduced. (a – d) correspond to experiments (3 – 6). (a), (b), and (d) show MoS_2 crystal growth on substrates placed in the middle of the furnace, while (c) shows no growth on a substrate placed further downstream.

Next, two growth experiments were performed utilizing the same growth conditions and different substrate placements and orientation with respect to the Ar flow. One substrate was placed face-down and in the middle of the furnace (60.5 cm), at the same position as the MoO_3 precursor and 45.5 cm from the S precursor. In contrast, the other substrate was placed face-up, slightly further downstream (75.5 cm) from the entrance (15 cm away from centered MoO_3 precursor, 60.5 cm from S precursor) for simultaneous growth. The distance of 75.5 cm from the entrance was chosen because it is the mid-point between far down-stream where no growth occurred (83.5 cm away, Figure 9c), and the middle of the furnace (60.5 cm from entrance) where growth occurred. Other parameters were kept constant with 0.5 g and 0.05 g for S and MoO_3 precursors, the argon flow rate of 25 sccm, and a growth chamber pressure of ~230 mTorr. Figure 10 shows the resulting MoS_2 growth from these conditions.

Both Figures 10a and 10b show uniform deposition compared to previous experiments indicating fewer layers of MoS_2. Furthermore, MoS_2 deposition was observed for the substrate placed face-up, further down-stream (Figure 10b) compared to the substrate placed in the middle of the furnace (Figure 10a). In comparing the two orientations, the substrate placed at 75.5 cm downstream was placed face-up to maximize the surface area of the vapor exposure on the substrate surface. In contrast, the substrate placed in the middle of the furnace (overhanging the MoO_3 precursor, 60.5 cm downstream) was placed faced-down to expose the substrate to MoO_3 vapor. Raman analysis shows Raman active peaks at ~381 – 383 cm^{-1} and ~405 – 407 cm^{-1} for E^1_{2g} and A_{1g} modes respectively, confirming MoS_2 crystal deposition.

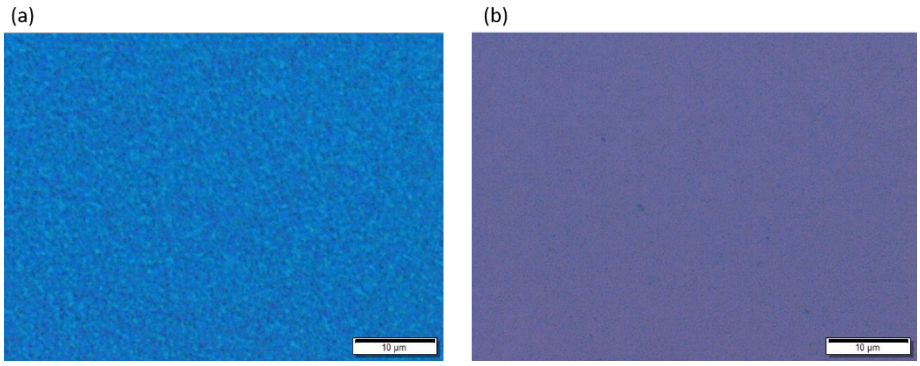

Figure 10. Optical microscope images (100x) of MoS_2 crystal growth from experiment 7. (a) corresponds to substrate placed at the center of the tube, the same location as the MoO_3 precursor, while (b) corresponds to the substrate placed 15 cm downstream from the MoO_3 powder (75.5 cm from the entrance). Both (a) and (b) show MoS_2 crystal deposition. The scale bar is 10 µm.

The resulting data show that the substrate distance from the MoO_3 precursor powder position plays a significant role in the deposition of MoS_2. It should be noted that the position of the S precursor was upstream and remained unchanged during this experimental set. The MoO_3 precursor was placed directly in the middle of the furnace (60.5 cm). Then, the SiO_2/Si substrate placement was varied from 0 (on top of the MoO_3 powder) to 15 cm further downstream. This modification caused MoS_2 crystal growth that was independent of the substrate orientation. However, when substrates were placed at a distance greater than 20 cm downstream (82 to 85 cm from the entrance) from the center, there was no MoS_2 growth (Figures 8 and 9c) indicating that we found the optimal precursor-substrate distance of 15 cm for the S precursor and 60.5 cm for the MoO_3 precursor.

For all of the experiments discussed above, an external heating belt was placed at the exposed part of the quartz tube near the gas entrance to sublimate the S precursor independently. However, as seen in Table 2, while the temperatures of each heating zones are controlled separately, the data indicates that residual heat from one zone affects the temperature profile of the adjacent zones. For instance, while the MoO_3 zone (Zone 2) was set to 850 ºC and the neighboring zones between room temperature (off) and 180 ºC, the heat from the higher temperature zone raised the temperature of the lower zone to 320 – 570 ºC significantly overshooting the S sublimation temperature. As such, the last set of MoS_2 growth utilized residual heat from the neighboring zone, rather than the heating belt to prevent overheating of the S precursor.

With the heating belt removed and the S substrate placed 30 cm from the entrance to compensate for the removal of direct heating of the S, optimized growth conditions from the previous experiment (0.5 and 0.05 g of S and MoO_3 precursors, argon gas flow of 25 sccm, ~230 mTorr internal pressure, and substrate positions of 60.5 and 75.5 cm), was utilized for MoS_2 crystal growth. Figures 11a and b show uniform dispersion of MoS_2 crystals compared to the previous experiments. Additionally, Figure 11c shows MoS_2 growth with the S precursor moved back to the initial position (15 cm from the entrance), indicating that the movement of the S precursor did not affect the overall quality of the MoS_2 crystal growth. The accompanying Raman analysis shows active peaks at ~383 cm^{-1} and ~405 cm^{-1} for E^1_{2g} and A_{1g} modes. As the MoS_2 growth produced a

thinner structure, the out-of-plane, A_{1g} peak shifted towards lower wavenumbers as less interlayer perturbation occurs, approaching the 402 cm^{-1} observed in monolayer MoS_2.

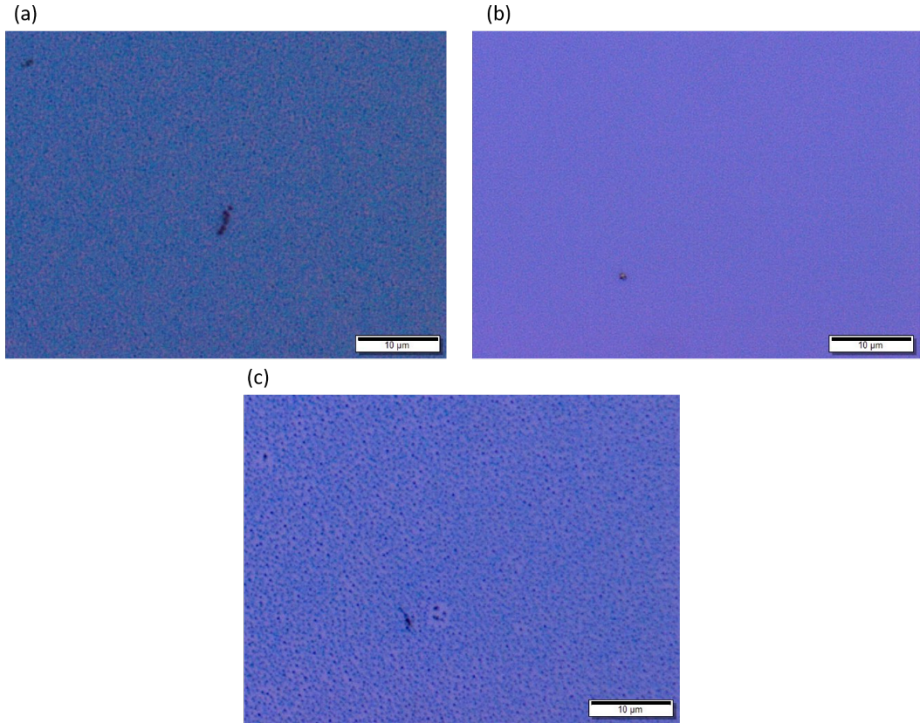

Figure 11. Optical microscope images (100x) of MoS_2 crystal growth with the heating belt removed. From experiments 8 and 9. (a) and (b) correspond to experiment 8, while (c) corresponds to experiment 9. All three substrates show thin MoS_2 crystal growth. The scale bar is 10 µm.

3.2 Number of Layers of MoS_2

Raman spectra of MoS_2 films can be used to determine the number of layers of MoS_2[32,40–43]. Specifically, the intralayer vibrational modes in MoS_2 crystals are affected by the thickness of the sample. As additional layers are introduced, the van der Waals bonded layers tend to "stiffen"[42] and as such, a shift in the peak location (Δfrequency) of the vibrational modes is observed. The lower in-plane vibrational E^1_{2g} mode is shifted to a lower frequency while the out-of-plane, A_{1g} mode is moved to a higher frequency with increasing MoS_2 crystal thickness[9,42]. Thus, the peak frequency difference ($A_{1g} - E^1_{2g}$) can be correlated to the thickness of the MoS_2 crystals. Figure 12 and Table 4 depict a correlation between frequency differences and the number of MoS_2 layers based on literature data[32,40–43].

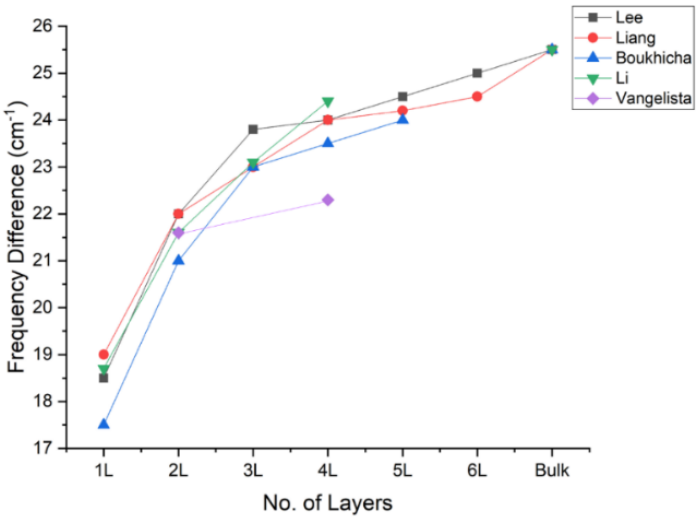

Figure 12. Peak frequency difference (A_{1g} - E^1_{2g}) peaks as a function of the number of layers for MoS_2 crystals obtained from literature: Liang[32], Vangelista[40], Li[41], Lee[42], Boukhicha[43].

Table 4. Average literature values of frequency difference (E^1_{2g} and A_{1g}) Raman modes as a function of the number of layers of MoS_2.

Literature values: Δfrequency ($A_{1g} - E^1_{2g}$)						
	Lee[42]	Liang[32]	Boukicha[43]	Li[41]	Vangelista[40]	Average
1L	18.5	19	17.5	18.7		18.42 ± 0.65
2L	22	22	21	21.6	21.6	21.64 ± 0.41
3L	23.8	23	23	23.1		23.30 ± 0.39
4L	24	24	23.5	24.4	22.3	23.64 ± 0.81
5L	24.5	24.2	24	25.5		24.55 ± 0.67
6L	25	24.5				24.75 ± 0.35
Bulk	25.5	25.5	25.5			25.50 ± 0.00

From Table 4, the average literature Δfrequency value of monolayer (1L) MoS_2 is 18.42 cm^{-1}. With an increasing number of layers, the frequency difference value increases from 21.64 to 24.75 cm^{-1} for bi- to six- MoS_2 layers respectively, while the frequency difference value for bulk MoS_2 is 25.50 cm^{-1}. From these literature values, the number of layers of our grown MoS_2 crystals can be estimated as well - the results are shown in Figure 13 and Table 5.

It should be noted that the Raman data presented in this report are different from those reported in the literature due to differing MoS_2 synthesis methods. These methods varied from mechanical exfoliation[41,42], electron beam evaporation[40], and modeled via density functional theory[32,43]. While some Raman analysis has been performed on CVD grown monolayer MoS_2, a systematic thickness analysis from CVD synthesized MoS_2 is not well established. As such, the synthesis method, involving different growth mechanisms, different substrate types, etc. should be considered when interpreting Raman data. For example, in graphene, the locations and the width of its signature Raman peaks vary depending on the substrate type, e.g., SiO_2/Si, Al_2O_3, polymers[44], synthesis method (e.g., exfoliation from HOPG, CVD, or epitaxial[45] growth), and the number of graphene layers[46].

For CVD grown monolayer MoS_2, the two characteristic Raman peaks are observed at 382 cm^{-1} and 402 cm^{-1} with the frequency difference of 20 cm^{-1} between the two peaks[9]. This value is approximately 1 cm^{-1} greater than the monolayer MoS_2 synthesized by other synthesis methods such as exfoliation presented in Table 4[8,9,12,47–49]. This difference is attributed to the different MoS_2 deposition process. In CVD growth, MoS_2 deposition occurs via nucleation of Mo and S vapors on the silicon substrate. In the mechanical exfoliation method, a layer (or layers) of MoS_2 is "pulled" away from an existing bulk structure. This perturbation of the plane in the exfoliation method, combined with possible crystalline imperfections in CVD synthesized films, result in a difference of the out-of-plane vibrational mode (A_{1g}) between CVD and exfoliated MoS_2[12,36]. Thus, in analyzing frequency differences for the data, it is acceptable to take our values and estimate within ~1 cm^{-1}, resulting in even thinner MoS_2 films compared to the initial estimate.

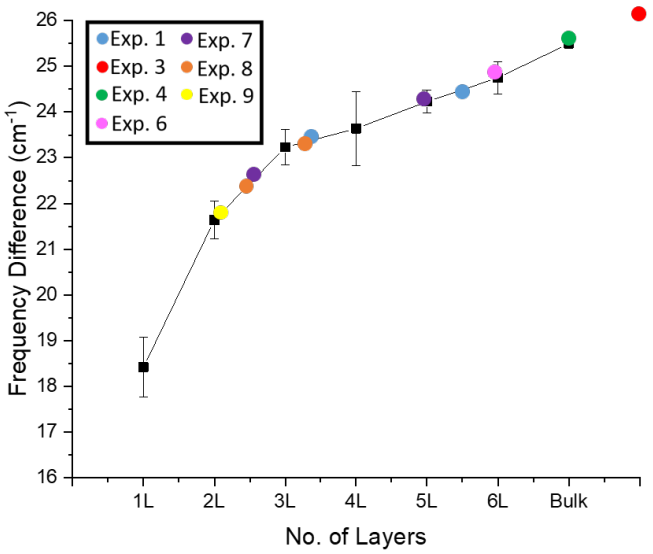

Figure 13. Estimation of the number of MoS_2 layers synthesized compared to the literature values. The black points indicate the frequency difference obtained from the literature values in Table 4.

Table 5. Average frequency difference values for synthesized MoS_2, with the number of layers, interpolated from the graph in Figure 12. The color of the table cells corresponds to experimental growth modified.

Experiment #	1	1	3	4	6	7	7	8	8	9
Δfrequency ($A_{1g} - E^1_{2g}$)	23.64 ± 0.81	24.55 ± 0.82	26.95 ± 0.81	25.55 ± 0.82	24.83 ± 0.83	24.11 ± 1.16	22.70 ± 0.00	22.34 ± 1.34	23.40 ± 1.00	21.99 ± 1.83
No. of Layers	3 - 4	5 - 6	Bulk	Bulk	6	5	2 - 3	2 -3	2 - 3	2 - 3

Peak frequency difference values obtained from the initial experiments with highest precursor amounts of 1 and 0.5 g of S and MoO_3, respectively, and higher argon gas flow rate (pressure) of 50 sccm (~377 mTorr) and the growth substrate placement in the middle of the furnace (same zone as MoO_3) are highlighted in red columns (experiment 1) in Table 5. When comparing these values to the literature values in Table 4, three to six layers of MoS_2 were estimated. The Raman analysis, as well as the accompanying optical analysis in Figure 6, confirm this observation. After the subsequent lowering of the gas flow rate (pressure) to 25 sccm (~230

mTorr) as well as reducing the amount of precursor powders by a factor of two for S and ten for MoO_3, the resulting peak frequency differences are 26.95 cm^{-1}, 25.55 cm^{-1}, 24.83 cm^{-1}, and 24.11 cm^{-1}, highlighted green in Table 5 (experiments 3, 4, 6, 7). These values indicate the presence of 5 layer to bulk MoS_2. The optical image in Figure 9 and Figure 10a confirm thick crystalline films with large particles several microns in size.

Next, utilizing the same conditions as the previous experiment but placing the growth substrate further downstream (75.5 cm from the entrance) from the MoO_3 precursor, a thinner deposition was observed with a peak frequency difference value of 22.70 cm^{-1}, highlighted blue in Table 5 which indicates a two to three layers thick film (experiment 7). The optical image in Figure 10b confirms this observation.

Lastly, utilizing the optimized conditions established from the previous experiments but with the heating belt removed, consistent synthesis of two to three layers of MoS_2 crystals was observed with corresponding Raman peak frequency differences of 22.34 cm^{-1}, 23.40 cm^{-1}, and 21.99 cm^{-1} highlighted yellow in Table 5 (experiments 8 and 9). By removing the heating belt and allowing the residual heat to sublimate the S precursor, more uniform sublimation of S occurred resulting in a more consistent film deposition.

4. SUMMARY

A systematic approach for growing two to three-layer thin MoS_2 crystals on SiO_2/Si substrates in a low-pressure chemical vapor deposition (LPCVD) system is presented in this report. The pretreatment of SiO_2/Si substrate via oxygen plasma, subsequent substrate and the precursor powder placements in the reactor, and the modifications of the experimental parameters such as precursor powder amount, internal chamber pressure, and the utilization of an external heating belt for S sublimation all affected the quality, as well as the thickness, of the resulting MoS_2 crystals. The MoS_2 crystal growth was qualitatively verified via optical microscopy in which clear, crystal deposition was observed. The growth was also confirmed by Raman spectroscopy to identify two characteristic Raman active bands, the lower in-plane, E^1_{2g} (382cm^{-1}), and out-of-plane A_{1g} (402 cm^{-1}) modes. Additional Raman analysis was performed to estimate the number of layers of MoS_2 crystals were grown by taking the difference in the peak positions of the two Raman active peaks.

Four layer to bulk MoS_2 were grown on SiO_2/Si substrates initially. Subsequently, with the optimization of the growth parameters such as the reduction in precursor amount, argon gas flow, internal chamber pressure, and the removal of the external heating belt, consistently thinner growth, ranging between two to three layers, was achieved. Raman analysis indicated that as the synthesis method is optimized, the out-of-plane interlayer mode red-shifted from ~ 407 cm^{-1} to ~ 404 cm^{-1} indicating less perturbation along the z-plane due to fewer number of layers present. Although the detailed mechanism of the MoS_2 crystal deposition with respect to the various experimental parameters is not yet elucidated, this work provides a basis for future modifications for thinner crystal growth of not only MoS_2 but other transition metal dichalcogenides utilizing LPCVD for various applications in 2D optoelectronic devices and applications.

ACKNOWLEDGEMENTS

This work was supported by the Office of Naval Research through the Naval Research Laboratory Base Program under the National Research Council Research Apprenticeship Program (NRC-RAP).

REFERENCES

1. Mak, K. F., Lee, C., Hone, J., Shan, J. & Heinz, T. F. Atomically Thin MoS_2: A New Direct-Gap Semiconductor. *Phys. Rev. Lett.* **105**, 136805 (2010).
2. Hu, T., Li, R. & Dong, J. A new (2 × 1) dimerized structure of monolayer 1T-molybdenum disulfide, studied from first principles calculations. *J. Chem. Phys.* **139**, 174702 (2013).
3. Jariwala, D., Sangwan, V. K., Lauhon, L. J., Marks, T. J. & Hersam, M. C. Emerging device applications for semiconducting two-dimensional transition metal dichalcogenides. *ACS Nano* **8**, 1102 (2014).
4. Bao, W., Cai, X., Kim, D., Sridhara, K. & Fuhrer, M. S. High mobility ambipolar MoS_2 field-effect transistors: Substrate and dielectric effects. *Appl. Phys. Lett.* **102**, 042104 (2013).
5. Islam, M. R. *et al.* Tuning the electrical property via defect engineering of single layer MoS_2 by oxygen plasma. *Nanoscale* **6**, 10033 (2014).
6. Fuhrer, M. S. & Hone, J. Measurement of mobility in dual-gated MoS_2 transistors. *Nat. Nanotechnol.* **8**, 146 (2013).
7. Klein, J. *et al.* Site-selectively generated photon emitters in monolayer MoS_2 via local helium ion irradiation. *Nat. Commun.* **10**, 1 (2019).
8. Xu, H. *et al.* High-Performance Wafer-Scale MoS_2 Transistors toward Practical Application. *Small* **14**, 1803465 (2018).
9. Chen, X. *et al.* CVD-grown monolayer MoS_2 in bioabsorbable electronics and biosensors. *Nat. Commun.* **9**, 1690 (2018).
10. Palummo, M., Bernardi, M. & Grossman, J. C. Exciton Radiative Lifetimes in Two-Dimensional Transition Metal Dichalcogenides. *Nano Lett.* **15**, 2794 (2015).
11. Pham, T., Li, G., Bekyarova, E., Itkis, M. E. & Mulchandani, A. MoS_2 -Based Optoelectronic Gas Sensor with Sub-parts-per-billion Limit of NO_2 Gas Detection. *ACS Nano* **13**, 3196 (2019).
12. Yu, Y. *et al.* Controlled Scalable Synthesis of Uniform, High-Quality Monolayer and Few-layer MoS_2 Films. *Sci. Rep.* **3**, 1866 (2013).
13. Choi, W. *et al.* High-detectivity multilayer MoS_2 phototransistors with spectral response from ultraviolet to infrared. *Adv. Mater.* **24**, 5832 (2012).
14. Park, J., Mun, J., Shin, J. S. & Kang, S. W. Highly sensitive two dimensional MoS_2 gas sensor decorated with Pt nanoparticles. *R. Soc. Open Sci.* **5**, 1 (2018).
15. Yin, Z. *et al.* Single-layer MoS_2 phototransistors. *ACS Nano* **6**, 74 (2012).
16. Li, X. & Zhu, H. Two-dimensional MoS_2: Properties, preparation, and applications. *J. Mater.* **1**, 33 (2015).
17. Novoselov, K. S. *et al.* Electric field in atomically thin carbon films. *Science* **306**, 666 (2004).

18. Radisavljevic, B., Radenovic, A., Brivio, J., Giacometti, V. & Kis, A. Single-layer MoS_2 transistors. *Nat. Nanotechnol.* **6**, 147 (2011).

19. Ganatra, R. & Zhang, Q. Few-Layer MoS_2 : A Promising Layered Semiconductor. *ACS Nano* **8**, 4074 (2014).

20. Zeng, Z. *et al.* Single-layer semiconducting nanosheets: High-yield preparation and device fabrication. *Angew. Chemie - Int. Ed.* **50**, 11093 (2011).

21. Coleman, J. N. *et al.* Two-Dimensional Nanosheets Produced by Liquid Exfoliation of Layered Materials. *Science* **331**, 568 (2011).

22. Fu, D. *et al.* Molecular Beam Epitaxy of Highly Crystalline Monolayer Molybdenum Disulfide on Hexagonal Boron Nitride. *J. Am. Chem. Soc.* **139**, 9392 (2017).

23. Yue, R. *et al.* Nucleation and growth of WSe_2: enabling large grain transition metal dichalcogenides. *2D Mater.* **4**, (2017).

24. Vishwanath, S. *et al.* Comprehensive structural and optical characterization of MBE grown $MoSe_2$ on graphite, CaF_2 and graphene. *2D Mater.* **2**, 1 (2015).

25. Wu, S. *et al.* Vapor–Solid Growth of High Optical Quality MoS2 Monolayers with Near-Unity Valley Polarization. *ACS Nano* **7**, 2768 (2013).

26. Lee, Y. H. *et al.* Synthesis of large-area MoS_2 atomic layers with chemical vapor deposition. *Adv. Mater.* **24**, 2320 (2012).

27. Lin, Y. C. *et al.* Wafer-scale MoS_2 thin layers prepared by MoO_3 sulfurization. *Nanoscale* **4**, 6637 (2012).

28. Zhan, Y., Liu, Z., Najmaei, S., Ajayan, P. M. & Lou, J. Large-area vapor-phase growth and characterization of MoS_2 atomic layers on a SiO_2 substrate. *Small* **8**, 966 (2012).

29. Splendiani, A. *et al.* Emerging Photoluminescence in Monolayer MoS_2. *Nano Lett.* **10**, 1271 (2010).

30. Muñoz, R. & Gómez-Aleixandre, C. Review of CVD synthesis of graphene. *Chem. Vap. Depos.* **19**, 297 (2013).

31. Bhaviripudi, S., Jia, X., Dresselhaus, M. S. & Kong, J. Role of kinetic factors in chemical vapor deposition synthesis of uniform large area graphene using copper catalyst. *Nano Lett.* **10**, 4128 (2010).

32. Liang, L. & Meunier, V. First-principles Raman spectra of MoS_2, WS_2 and their heterostructures. *Nanoscale* **6**, 5394 (2014).

33. Bilgin, I. *et al.* Chemical Vapor Deposition Synthesized Atomically Thin Molybdenum Disulfide with Optoelectronic-Grade Crystalline Quality. *ACS Nano* **9**, 8822 (2015).

34. Wang, W. *et al.* Investigation of the Growth Process of Continuous Monolayer MoS_2 Films Prepared by Chemical Vapor Deposition. *J. Electron. Mater.* **47**, 5509 (2018).

35. Zhou, D. *et al.* Unveiling the Growth Mechanism of MoS_2 with Chemical Vapor Deposition: From Two-Dimensional Planar Nucleation to Self-Seeding Nucleation. *Cryst. Growth Des.* **18**, 1012 (2018).

36. Dumcenco, D. *et al.* Large-Area Epitaxial Monolayer MoS_2. *ACS Nano* **9**, 4611 (2015).

37. Shi, J. *et al.* Monolayer MoS2 growth on au foils and on-site domain boundary imaging. *Adv. Funct. Mater.* **25**, 842–849 (2015).

38. Shi, J. *et al.* Substrate facet effect on the growth of monolayer MoS_2 on Au foils. *ACS Nano* **9**, 4017 (2015).

39. Ji, Q. *et al.* Epitaxial monolayer MoS2 on mica with novel photoluminescence. *Nano Lett.* **13**, 3870–3877 (2013).

40. Vangelista, S. *et al.* Towards a uniform and large-scale deposition of MoS_2 nanosheets via sulfurization of ultra-thin Mo-based solid films. *Nanotechnology* **27**, 175703 (2016).

41. Li, H. *et al.* From Bulk to Monolayer MoS_2: Evolution of Raman Scattering. *Adv. Funct. Mater.* **22**, 1385 (2012).

42. Lee, C. *et al.* Anomalous Lattice Vibrations of Single- and Few-Layer MoS_2. *ACS Nano* **4**, 2695 (2010).

43. Boukhicha, M., Calandra, M., Measson, M.-A., Lancry, O. & Shukla, A. Anharmonic phonons in few-layer MoS_2: Raman spectroscopy of ultralow energy compression and shear modes. *Phys. Rev. B* **87**, 195316 (2013).

44. Wang, Y. Y. *et al.* Raman studies of monolayer graphene: The substrate effect. *J. Phys. Chem. C* **112**, 10637 (2008).

45. Wu, J. Bin, Lin, M. L., Cong, X., Liu, H. N. & Tan, P. H. Raman spectroscopy of graphene-based materials and its applications in related devices. *Chem. Soc. Rev.* **47**, 1822 (2018).

46. Park, J. S. *et al.* G′ band Raman spectra of single, double and triple layer graphene. *Carbon N. Y.* **47**, 1303 (2009).

47. Chen, X. *et al.* Lithography-free plasma-induced patterned growth of MoS_2 and its heterojunction with graphene. *Nanoscale* **8**, 15181 (2016).

48. Jeon, J. *et al.* Layer-controlled CVD growth of large-area two-dimensional MoS_2 films. *Nanoscale* **7**, 1688 (2015).

49. Zhang, X. *et al.* Raman spectroscopy of shear and layer breathing modes in multilayer MoS_2. *Phys. Rev. B* **87**, 115413 (2013).

APPENDIX

A. Raman peak analysis for all MoS_2 Crystals

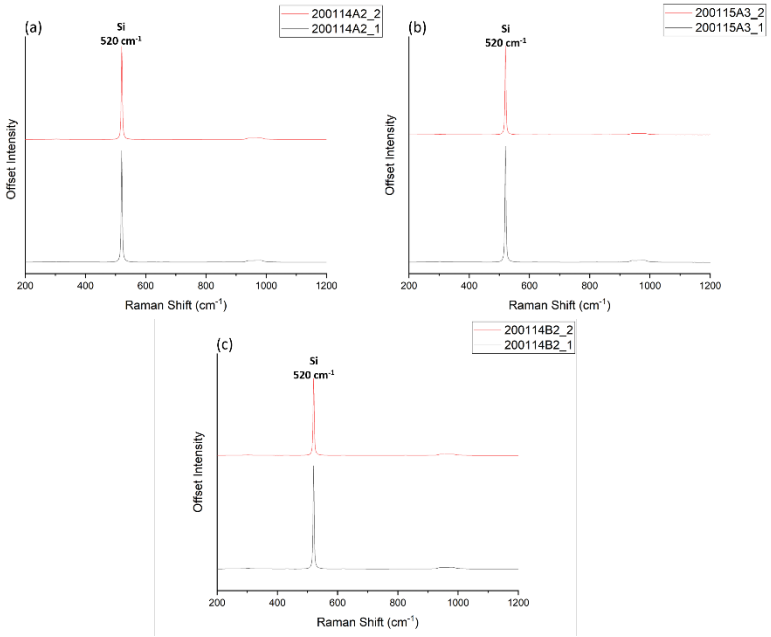

Figure A1. Raman spectroscopy data for experimental conditions that did not produce any MoS_2 growth. (a) and (b) correspond to experiment 2, while (c) corresponds to experiment 5. A sharp silicon substrate peak is observed at 520 cm^{-1}.

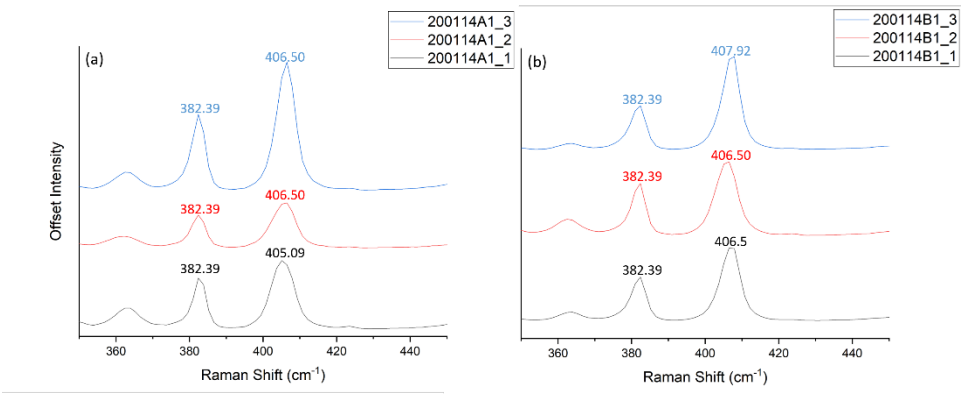

Figure A2. Raman spectroscopy data for experiment 1. (a) corresponds to 200114A1 and (b) corresponds to 200115B1. Different colors represent separate areas analyzed.

Table A1. Table summarizing Raman peak analysis for experiments 1.

			Peak Frequency (cm^{-1})		
	200114		E^1_{2g}	A_{1g}	Δfrequency (A_{1g} - E^1_{2g})
Exp. 1	A1	1	382.39	405.09	22.70
		2	382.39	406.50	24.11
		3	382.39	406.50	24.11
		X	382.39	406.03	23.64 ± 0.81
	B1	1	382.39	406.50	24.11
		2	382.39	406.50	24.11
		3	382.39	407.92	25.53
		X	382.39	406.97	24.58 ± 0.82

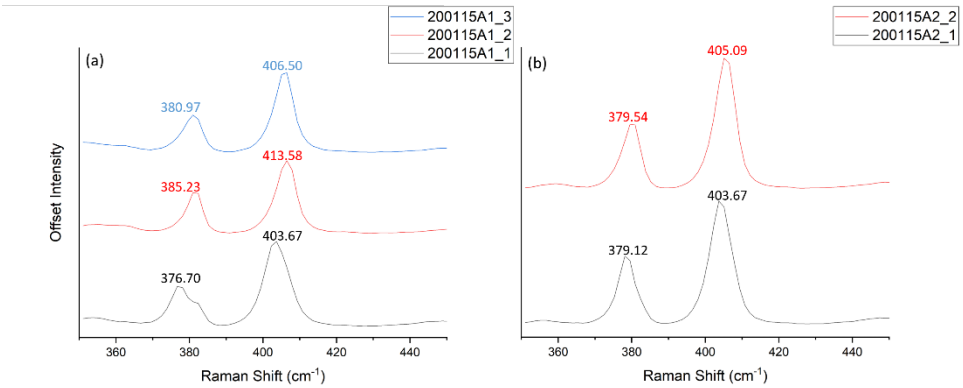

Figure A3. Raman spectroscopy data for experiments 3 and 4. (a) corresponds to 200115A1 and (b) corresponds to 200115A2. Different colors represent separate areas analyzed.

Table A2. Table summarizing Raman peak analysis for experiments 3 and 4.

			Peak Frequency (cm^{-1})		
	200115		E^1_{2g}	A_{1g}	Δfrequency (A_{1g} - E^1_{2g})
Exp. 3	A1	1	376.70	403.67	26.97
		2	385.23	413.58	28.35
		3	380.97	406.50	25.53
		X	380.97	407.92	26.95 ± 1.41
Exp. 4	A2	1	378.12	403.67	25.55
		2	379.54	405.09	25.55
		X	378.83	404.38	25.55 ± 0.00

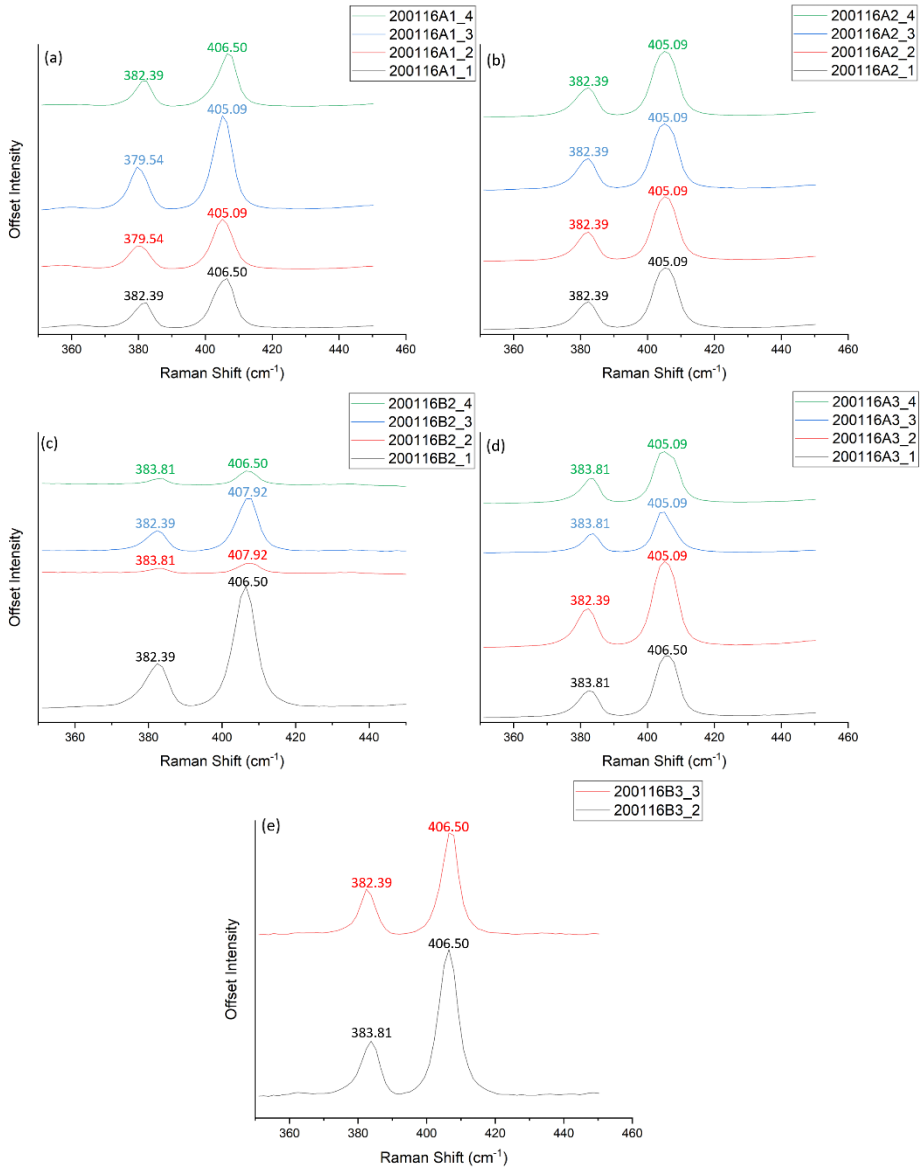

Figure A4. Raman spectroscopy data for experiments 6, 7, and 8: (a) 200116A1, (b) 200116A2, (c) 200116B2, (d) 200116A3, and (e) 200116B3. Different colors represent separate areas analyzed.

Table A3. Table summarizing Raman peak analysis for experiments 6, 7, and 8.

			Peak Frequency (cm^{-1})		
	200116		E^1_{2g}	A_{1g}	Δfrequency (A_{1g} - E^1_{2g})
Exp. 6	A1	1	382.39	406.50	24.11
		2	379.54	405.09	25.55
		3	379.54	405.09	25.55
		4	382.39	406.50	24.11
		X	380.97	405.78	24.83 ± 0.83
Exp. 7	A2	1	382.39	405.09	22.70
		2	382.39	405.09	22.70
		3	382.39	405.09	22.70
		4	382.39	405.09	22.70
		X	382.39	405.09	22.70 ± 0.00
	B2	1	382.39	406.50	24.11
		2	383.81	407.92	24.11
		3	382.39	407.92	25.53
		4	383.81	406.50	22.69
		X	383.10	407.21	24.11 ± 1.16
Exp. 8	A3	1	382.39	406.50	24.11
		2	382.39	405.09	22.70
		3	383.81	405.09	21.28
		4	383.81	405.09	21.28
		X	383.10	405.44	22.34 ± 1.34
	B3	1	383.81	406.50	22.69
		2	382.39	406.50	24.10
		X	383.10	406.50	23.40 ± 1.00

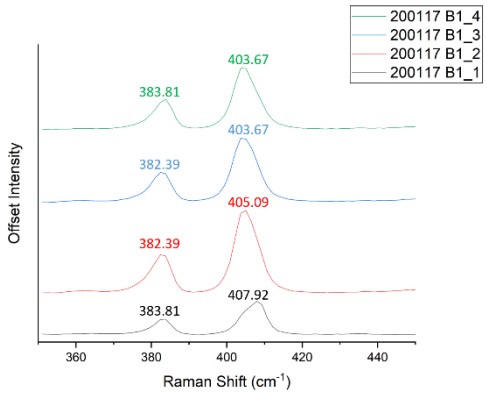

Figure A5. Raman spectroscopy data for experiment 9. The spectra correspond to 200117B1. Different colors represent separate areas analyzed.

Table A4. Table summarizing Raman peak analysis for experiment 9.

			Peak Frequency (cm^{-1})		
	200117		E^1_{2g}	A_{1g}	Δfrequency (A_{1g} - E^1_{2g})
Exp. 9	B1	1	383.81	407.92	24.11
		2	382.39	405.09	22.70
		3	382.39	403.67	21.28
		4	383.81	403.67	19.86
		X	383.10	405.09	21.99 ± 1.83